Journal of Materials Chemistry C

ROYAL SOCIETY OF CHEMISTRY

PAPER

View Article Online
View Journal | View Issue

Cite this: J. Mater. Chem. C, 2026, 14, 1933

Bifunctional $[Fe_6Co_7]$ cyanide bridged assemblies: electron transfer coupled spin transition and liquid crystal properties

Jyoti Yadav, [a] Ranjan Kharel, [a] Ritobrata De, [b] Santanu Kumar Pal, [b] Bhart Kumar, [a] Pradip Kumar Mondal [c] and Sanjit Konar *[a]

Received 12th September 2025,
Accepted 28th October 2025

DOI: 10.1039/d5tc03401a

rsc.li/materials-c

Mesostructuring of Prussian blue analogues (PBAs) can impart high surface area and anisotropic magnetic behavior, making them desirable for practical applications as switches, sensors and display devices. Herein, we present the first report of alkylated $\{[Fe_3Co_3]_2Co\}$ tridecanuclear PBAs exhibiting magnetic bistability co-existing with thermochromism (green → red) and crystal to liquid–crystal phase change. The rational design strategy led to the isolation of these tridecanuclear complexes with general formula $\{[Fe^{II}Tp(CN)_3]_3[Co^{III}(L\text{-}C_n)_2]_3\}_2Co^{II}\cdot A^-\cdot y$solvents (For **1**-$C_n$; A^- = $7BF_4^-\cdot[Fe^{III}Tp(CN)_3]^-$, y = $64H_2O$ and for **2**-C_n; A^- = $8ClO_4^-$, y = $8H_2O$), where n = carbon chain length, *i.e.* 4, 6, 8, 10, 12, 14, 16; Tp = hydrotris(1-pyrazolyl)borate and L-C_n = *N*-alkylated 2,2′-dipyridylamine with the respective carbon chain lengths. The transition and melting temperatures of the complexes are in synchronisation and decrease with increasing carbon chain length. This occurs due to higher flexibility of longer alkyl chains. The flexible chains not only induce liquid crystalline properties in the complexes, but also allow their fabrication into thin films with nearly no compromise in the magnetic bistability and thermochromic behavior. This strategy to functionalise PBAs with flexible alkyl chains provides an array of mesostructures with tunable magnetic, optical, and electronic properties.

Introduction

Molecular magnetic bistability represents one of the most compelling aspects in chemistry, with potential applications in high-density storage devices, switches, displays, and sensors.[1,2] Achieving bistability in metal complexes is primarily accomplished through (a) spin crossover (SCO) phenomena, characterized by interconversion between low-spin (LS) and high-spin (HS) states,[3] or (b) electron transfer (ET) phenomena,[4] in response to external stimuli such as temperature, pressure, light, or chemical stimuli.[5–9] Significant research has focused on the nanostructuring and processability of these bistable compounds to facilitate their integration into technological devices.[10,11] One effective approach involves modifying ligands with long alkyl chains, which confer low melting temperatures, high solubility, and amphiphilic properties, enabling the formation of liquid crystals (LCs), gels, films, and polymers.[12–15] The rational design of multifunctional materials that combine magnetic switchability with LC behavior is particularly attractive due to the variable spin states, magnetic anisotropy, and coordination flexibility of metal ions within the anisotropic phases.[14–17] The first report of an iron(III) complex exhibiting both SCO and LC properties was documented by Galyametdinov and co-workers, but the two phenomena were not synchronised.[18] Thereafter, only a limited number of studies have reported SCO events coupled with any extrinsic phase transitions.[19–22] In most cases, the melting of the complexes leads to structural modifications that influence ligand field strength and cooperative interactions between SCO centers.[12,19,23,24] Besides the investigation of bifunctionality in Fe(III/II) complexes with synchronised LC and SCO behavior, to the best of our knowledge, there are no reports combining LC properties with electron transfer processes. MacLachlan and co-workers reported the first mesostructured Prussian blue analogues (PBAs); however, these complexes lacked both spin-crossover (SCO) and electron transfer behavior.[25] The phenomenon of electron transfer coupled spin transition (ETCST) has gained significant attention in recent decades, particularly in [FeCo] PBAs, due to their unique intermetallic electron transfer through bridged cyanide groups.[4,26] No significant progress has been made in the development of alkyl chain-functionalized PBAs, which could yield easily processable

[a] Department of Chemistry, Academic Building-2 Indian Institute of Science Education and Research (IISER) Bhopal, Bhopal Bypass Road, Bhopal, Madhya Pradesh-462066, India. E-mail: skonar@iiserb.ac.in
[b] Department of Chemical Sciences, Indian Institute of Science Education and Research (IISER), Mohali Sector 81, SAS Nagar, Knowledge City Manauli, Punjab-140306, India. E-mail: skpal@iisermohali.ac.in
[c] Elettra – Sincrotrone Trieste S.C. p. A., S.S. 14, Km 163.5 in Area Science Park, Basovizza 34149, Italy

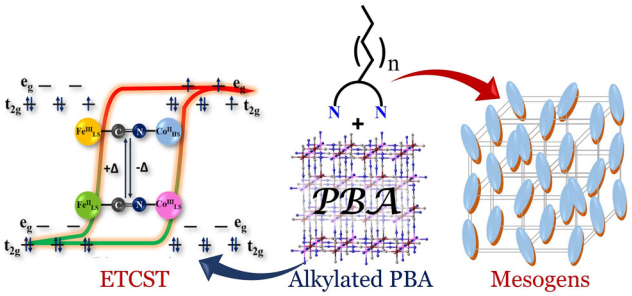

Scheme 1 Representation of the designed bifunctional Prussian blue analogues using alkyl chain functionalized capping ligands that may give rise to mesogenic/liquid crystal properties along with thermochromic and ETCST behavior.

materials with thermo-/photochromic properties and electron transfer coupled magnetic switchability, enhancing their potential for practical applications.

We focused on functionalizing the [FeCo] cyanide-bridged system with long alkyl chains to explore bifunctionality in PBAs. This effort of rational design and synthesis led to the isolation of a series of discrete tridecanuclear [Fe_6Co_7] PBAs decorated with alkyl chains of varying lengths (C_n; n = 4, 6, 8, 20, 12, 14 and 16) (Scheme 1). All the complexes exhibited ETCST behavior at their melting points and demonstrated thermochromic properties. Interestingly, the complex **1**-C_{16} with comparatively longer alkyl chains was observed to exhibit a columnar hexagonal (Col_h) mesophase, which subsequently underwent a phase transition to a glassy state, synchronised with the ETCST phenomenon.

Results and discussion

Synthetic procedures

All complexes **1**-C_n were synthesised from a CH_3OH solution containing the respective alkyl-substituted capping ligand (*N*-alkyl-*N*-(pyridin-2-yl)pyridin-2-amine, L-C_n), $Co(BF_4)_2{\cdot}6H_2O$, and $Na[Fe^{III}Tp(CN)_3]$. Solutions with n = 4 and 6 carbon chains produced a clear dark green color, which upon slow evaporation yielded block-shaped and plate-like crystals, respectively. In contrast, the reaction mixtures with longer alkyl chains (n = 8, 10, 12, 14, and 16) resulted in a dark green precipitate.

Structural analysis of complex **1**-C_4 was performed using single-crystal X-ray diffraction, but the poor crystal quality of complex **1**-C_6 led to weak diffraction, limiting its structural study. With a similar synthetic procedure, a series of complexes $\{[Fe^{II}Tp(CN)_3]_3[Co^{III}(L\text{-}Cn)_2]_3\}_2Co^{II}{\cdot}8ClO_4{\cdot}8H_2O$ (**2**-C_n) were synthesised using $Co(ClO_4)_2{\cdot}6H_2O$, $Na[Fe^{III}Tp(CN)_3]$ and the alkylated dpa ligands with even carbon chain lengths (n = 4–16). The structural analysis of complex **2**-C_4 was conducted using synchrotron X-ray diffraction and further details are provided in the SI.

Structural description

The single-crystal structural analysis of complex **1**-C_4 at 100 K, revealed the formation of $\{[Fe^{II}Tp(CN)_3]_3[Co^{III}(L\text{-}C_4)_2]_3\}_2Co^{II}$. $7BF_4{\cdot}[Fe^{III}Tp(CN)_3]{\cdot}64H_2O$, crystallizing in the triclinic $P\bar{1}$ space group (Fig. 1a). This complex, with a simplified molecular framework of $[Fe_3(\mu\text{-}CN)_6Co_3(CN)]_2(\mu\text{-}CN)_4Co$, consists of two hexanuclear cyclic rings (I and II) resembling a distorted boat-like conformation (Fig. 1b). Each cyclic ring comprises three $[Co(L\text{-}C_4)_2]$ and three $[FeTp(CN)_3]$ subunits positioned alternately and linked *via* cyanide groups. Two cyanide groups from each $[FeTp(CN)_3]$ are involved in bridging with the $[Co(L\text{-}C_4)_2]$ subunits, forming the hexanuclear cyclic ring. The third cyanide group of Fe1 and Fe3 of the $[FeTp(CN)_3]$ subunits bridges to a tetrahedral Co center (Co4), which links the two cyclic rings. The remaining cyanide group of Fe2 is non-bridged (terminal) and is oriented outward from the ring (Fig. 1b). Only the tetrahedral Co4 center is in an N_4 coordination environment, while the remaining Co and Fe centers are in N_6 and C_3N_3 coordination environments, respectively (Fig. 1). The crystallographic details are provided in the SI.

The average Fe–C and Fe–N bond lengths for all the Fe centers were found to be 1.86 Å and 1.988 Å, respectively, indicating that the Fe ions are in the 2+ low-spin (LS) state. And, the average Co–N bond lengths of ~1.921 Å for Co1, Co2, and Co3 are consistent with Co ions in the 3+ low-spin (LS) state. Thus, the Fe and Co centres of the hexanuclear cyclic rings are in the $[Fe^{II}_{LS}(\mu\text{-}CN)Co^{III}_{LS}]$ diamagnetic electronic configuration.[27] The Co4–N bond length ranges between 1.953–1.974 Å suggesting the 3+ LS state (bond length considerations), while the tetrahedral geometry suggests a 2+

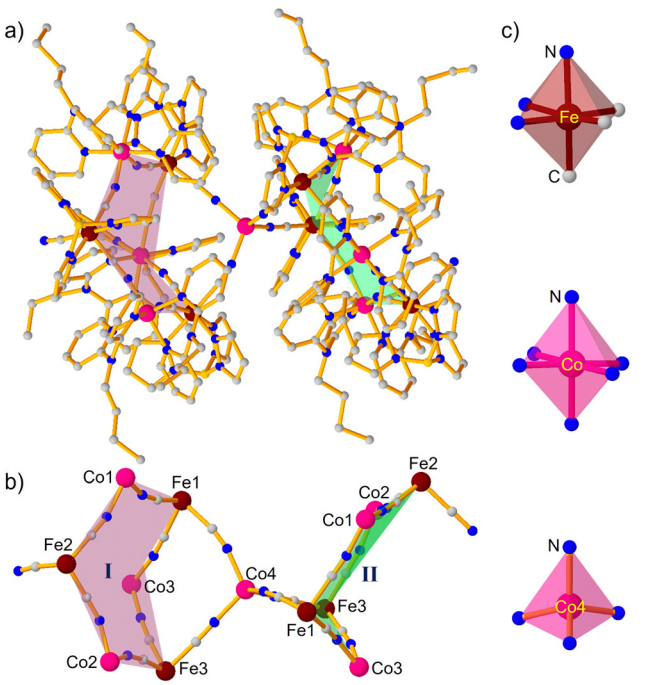

Fig. 1 (a) Structure of **1**-C_4, (b) simplified structure of **1**-C_4 showing only the structural framework of the tridecanuclear complex with two hexanuclear rings I and II, and a central tetrahedral Co4 metal ion bridging the two rings *via* cyanide groups and (c) the coordination environment of all the Fe(1,2,3), Co(1,2,3) and Co4 metal centres. Color code: Fe (brown), Co (pink), N (blue), B (yellow) and C (grey).

high-spin (HS) state. Therefore, given that the complete structure contains seven BF_4^- ions (6 assigned and 1 masked) and one non-bridged $[FeTp(CN)_3]^-$ unit, resulting in a total of eight anions in the crystal lattice, the Co4 ion is supposed to be in the 2+ oxidation state to make a charge neutral molecule (comprising $6Fe^{II}$, $6Co^{III}$, and $1Co^{II}$). Additionally, due to its tetrahedral geometry, the Co4 ion can be assigned to the HS state. Overall, the complete molecular structure has two hexanuclear cyclic rings (diamagnetic, $6Fe^{II}_{LS}$, $6Co^{III}_{LS}$) and Co4 as the only magnetically active center present in the framework, along with the non-bridged $[FeTp(CN)_3]^-$ units present in the lattice. The complex formed extensive intramolecular and intermolecular π–π interactions varying with a distance of 3.538–3.828 Å, between the pyridine rings of the coordinated dpa ligands and the pyrazolyl rings of the bridged and non-bridged $[FeTp(CN)_3]$ subunits (SI, Fig. S4).

Due to the reduced crystallinity for the complexes with long alkyl chain lengths, the structural characterizations of these complexes were performed using spectroscopic techniques. The similar vibrational peaks and electronic absorption bands in the infrared and UV-Visible spectra, respectively, indicate the isostructural and isoelectronic nature of complex **1**-C_4 with its high alkyl chain substituted analogues (SI, Fig. S7–S10).

Magnetic property study

The magnetic measurement of complexes **1**-C_n was performed using a SQUID magnetometer at 10 000 Oe applied DC field. At 300 K, the $\chi_M T$ value of complex **1**-C_{16} was observed to be 3.39 cm^3 K mol^{-1}, which corresponds to the presence of Co4 in the Co^{II}_{HS} (S = 3/2) state and one Fe^{III}_{LS} (S = 1/2) of a non-bridged $[FeTp(CN)_3]^-$ anion. This confirms the $[Fe^{II}_{LS}(\mu\text{-}CN)Co^{III}_{LS}]_3$ diamagnetic pairs in the hexanuclear cyclic rings, and the electronic configuration of the complex can be represented as $\{[Fe^{II}_{LS}(\mu\text{-}CN)Co^{III}_{LS}]_3\}_2Co^{II}_{HS}$. With increasing temperature, the $\chi_M T$ value shows a gradual increase to 6.35 cm^3 K mol^{-1} until 450 K, which further increases very abruptly to 24.53 cm^3 K mol^{-1} above 476 K. The $\chi_M T$ value at 476 K corresponds to the presence of seven Fe^{III}_{LS} (S = 7/2) and seven Co^{II}_{HS} (S = 21/2) with significant spin–orbit coupling. Hence, the abrupt transition indicates the occurrence of the ETCST phenomenon in the complex with one electron transfer from the Fe^{II}_{LS} to the Co^{III}_{LS} followed by the spin transition at the Co-centre to Co^{II}_{HS}. Here, the Co4 centre is expected to retain its 2+ HS electronic state, while the ETCST phenomenon is expected to occur exclusively in the two cyclic hexanuclear rings I and II. The overall electronic states for the metal centres can be represented as $\{[Fe^{III}_{LS}(\mu\text{-}CN)Co^{II}_{HS}]_3\}_2Co^{II}_{HS}$. Additionally, the gradual increase of $\chi_M T$ between 400–450 K is anticipated for the reorientation of the highly flexible long alkyl chains, which leads to phase transition.[15] During the cooling mode, a constant $\chi_M T$ value of ~24.56 cm^3 K mol^{-1} was observed up to 300 K representing the paramagnetic $\{[Fe^{III}_{LS}(\mu\text{-}CN)Co^{II}_{HS}]_3\}_2Co^{II}_{HS}$ state of the complex. Hence, the magnetic susceptibility measurement revealed the irreversible ETCST in the complex **1**-C_{16} (Fig. 2).

For the complexes **1**-C_n with different alkyl chain lengths, a similar irreversible high-temperature abrupt ETCST phenomenon

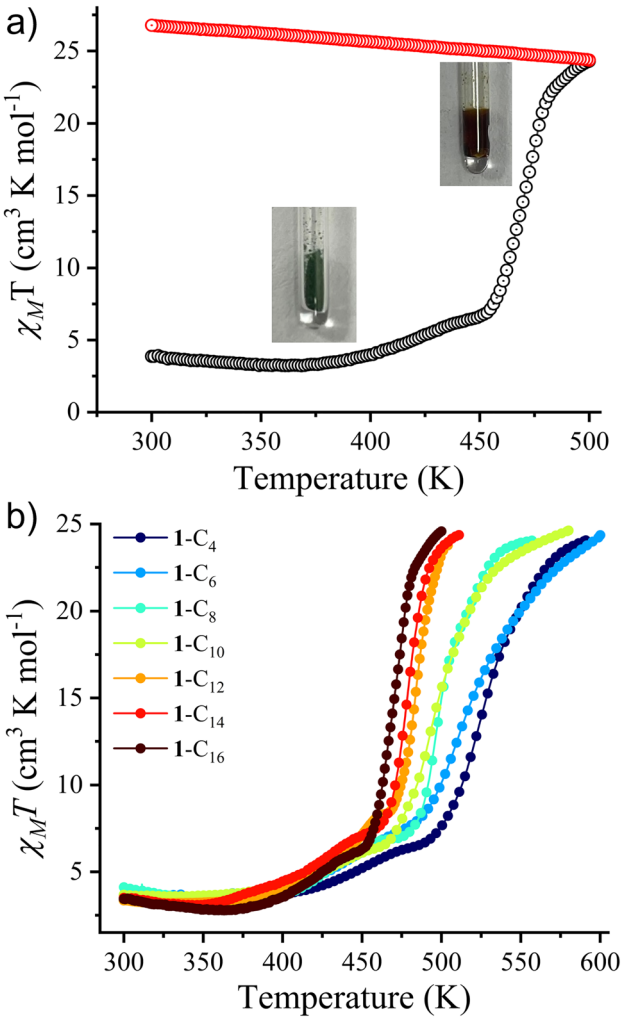

Fig. 2 (a) $\chi_M T$ *vs.* temperature plot for complex **1**-C_{16} during heating (black) and the cooling mode (red); the inset shows the color and the nature of the sample during measurement of the melting point and (b) $\chi_M T$ *vs.* temperature plots for the complexes **1**-C_n with varying alkyl chain lengths in the heating mode at a scan rate of 3 K min^{-1} and 1 T applied magnetic field.

was observed. However, with an increase in the alkyl chain lengths, the electronic transitions ($T_{1/2}$) shift to lower temperatures (Fig. 3 and Table S9). The ETCSTs in each complex co-exist with their respective melting temperatures. The higher alkyl chain lengths impart more flexibility into the system, resulting in lower melting temperatures. Therefore, the inverse relation of $T_{1/2}$ with the alkyl chain length can be attributed to the change in the melting temperatures of the complexes.

Physical property study

The magnetic transitions observed for the complexes **1**-C_n were accompanied by an irreversible thermochromic behaviour (dark green → red) in the solid state, which is due to the different absorption patterns of the two distinct electronic configurations. The spectroscopic studies of the freshly prepared green samples showed ν_{CN} at 2071, 2094 and 2120 cm^{-1}

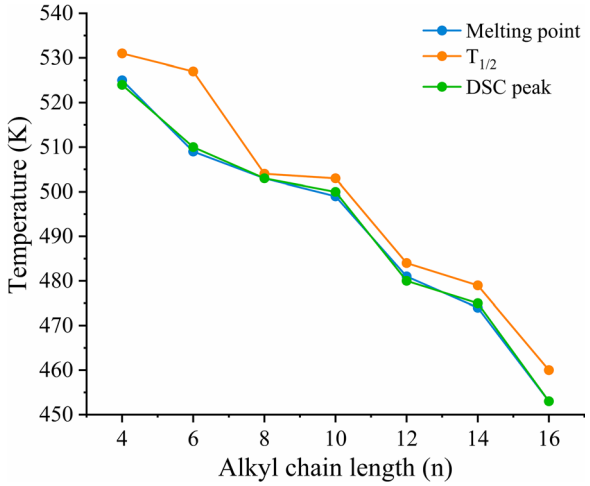

Fig. 3 Graphical representation of melting points, $T_{1/2}$ and DSC peaks with respect to the alkyl chain lengths for the complexes **1**-C_n (n = 4, 6, 8, 10, 12, 14 and 16).

and ν_{BH^-} at 2478 cm^{-1} representing $[Fe^{II}_{LS}(\mu\text{-CN})Co^{III}_{LS}]$ diamagnetic pairs, while heating resulted in conversion to the red phase with a shift in stretching frequencies to a higher wavenumber (ν_{CN} at 2149 and 2156 cm^{-1} and ν_{BH^-} at 2510 cm^{-1}) corresponding to the formation of the $[Fe^{III}_{LS}(\mu\text{-CN})Co^{II}_{HS}]$ paramagnetic phase (Fig. 4a).[6a] Similarly, the solid-state UV-visible spectra showed the presence of a metal-to-metal-charge transfer (MMCT) band at 650 and 740 nm in the as synthesised complexes. However, these bands diminished with the emergence of a new MMCT band at 480 nm upon heating to their melting temperatures (Fig. 4b). The dehydrated solid samples (red products) upon rehydration didn't revert to their original green-colored state, indicating that the dehydration–rehydration process is irreversible.

Interestingly, a reversible thermochromic phase conversion of the complexes was observed in the solution (green $(\{[Fe^{II}_{LS}(\mu\text{-CN})Co^{III}_{LS}]_3\}_2Co^{II}_{HS}) \leftrightarrow$ red $(\{[Fe^{III}_{LS}(\mu\text{-CN})Co^{II}_{HS}]_3\}_2Co^{II}_{HS})$. Additionally, the ETCST and thermochromism in complexes **1**-C_n occur at lower temperatures in contrast to the solid-state transitions (Fig. 4c and Fig. S11).

The irreversibility of the structural phase transition and the ETCST property of the complex **1**-C_{16} in the solid state were further justified by the presence of endothermic peaks and the absence of exothermic peaks in the DSC thermogram (Fig. 5a and Fig. S14). For complexes with smaller alkyl chains (**1**-C_4, **1**-C_6 and **1**-C_8), an exothermic peak was observed, corresponding to solidification of the melted sample, while for complexes with higher alkyl chains (**1**-C_{10}, **1**-C_{12}, **1**-C_{14} and **1**-C_{16}) the complexes remain in the glassy phase. The endothermic peak in the DSC thermograms during the heating mode reveals small discrepancies in the transition temperatures of the complexes compared to those observed in the magnetic measurements. These are likely attributed to the effect of applied pressure during the preparation of pellets from the powdered samples for high-temperature magnetic measurements. The thermal stability and decomposition temperatures for all the complexes were evaluated by thermogravimetric analysis (TGA) (Fig. S15 and S16).

Following the DSC thermograms, where the complexes with higher alkyl chains are more prone to show the existence of an intermediate phase, the complex **1**-C_{16} was chosen as the representative compound for extensive studies regarding the presence of the LC phase. A narrow range of temperature was observed between the two endothermic peaks for complex **1**-C_{16}, which indicated phase transitions with considerable low values of enthalpy change, characteristic of the LC phase. Hence, polarised optical microscopy (POM) images for the complex **1**-C_{16} were recorded during both heating and cooling cycles. It was observed that during the first heating cycle, a crystalline to LC phase transition occurred at 493 K. The shearable birefringence pattern was typical of that of a columnar mesophase (Fig. 5c(i)–(iii)).

However, upon subsequent heating, instead of attaining the isotropic phase, the sample assumed an immovable glassy phase at 521 K. During the cooling cycle, the reappearance of the birefringent textures was not observed, and the glassy phase persisted until room temperature (Fig. 5c(iv)–(vi)). This glassy phase continued through the second heating cycle as well, and neither the crystalline nor the LC properties were restored in

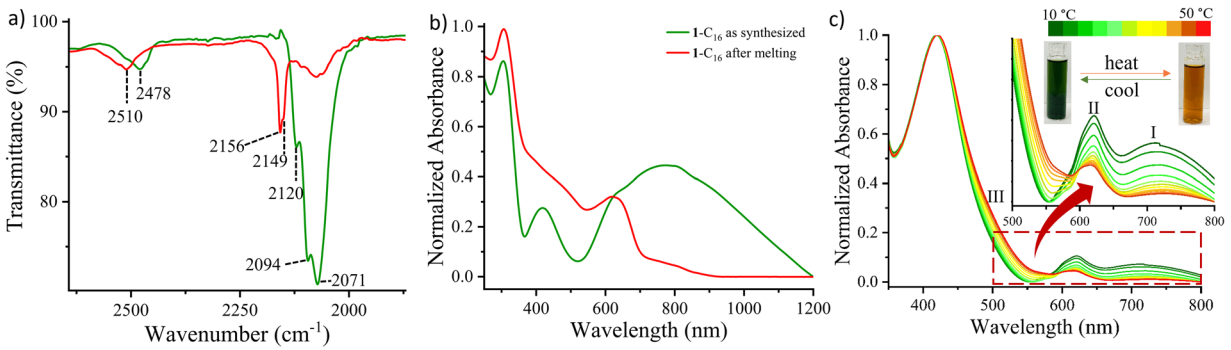

Fig. 4 (a) Infrared and (b) solid state UV-visible spectroscopy of complex **1**-C_{16} for the fresh (green) and heated (red) sample, and (c) variable temperature UV-visible spectrum of complex **1**-C_{16} in methanol; MMCT bands at I correspond to $[Fe^{II}_{LS}(\mu\text{-CN})Co^{III}_{LS}]$, II is assumed for $[Fe^{II/III}_{LS}(\mu\text{-CN})Co^{II}_{HS}]$ (for Co_4) and III shows the appearance of MMCT for $[Fe^{III}_{LS}(\mu\text{-CN})Co^{II}_{HS}]$. The colour change behavior in the solid and solution phases is shown in the insets of (b) and (c) UV-visible spectra, respectively.

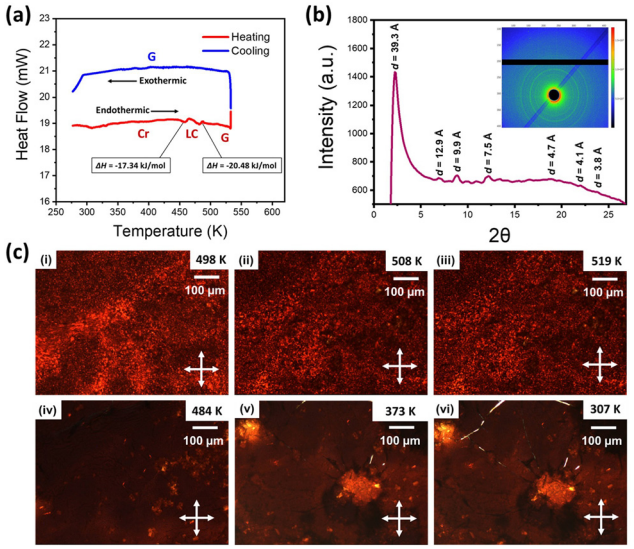

Fig. 5 (a) DSC thermogram of complex **1**-C_{16} showing the first heating and cooling cycles (phases: Cr = crystalline; LC = liquid crystal; G = glassy), (b) X-ray scattering pattern of **1**-C_{16} in its mesophase, recorded at 493 K during the heating cycle, where 2θ is in degrees and d-spacing values are in Å (inset: 2D diffraction pattern). (c) POM textures of **1**-C_{16} during heating mode (i–iii) and during cooling mode (iv–vi).

the material, making it a monotropic LC. The inferences from the POM studies corroborated with the preliminary observation from DSC, wherein the slight difference in the transition temperatures obtained from the two different methods can be attributed to the difference in experimental conditions (while DSC is carried out in a completely inert closed atmosphere, POM images are recorded in an open hot-stage). This observation was fully supported by DSC, where the enthalpy changes were much lower than the crystal-isotropic transitions (which generally have values above 35 kJ mol^{-1}), with the crystal-LC and LC-glassy state transition enthalpies of 17.34 and 20.48 kJ mol^{-1}, respectively. These fall well within the range of mesophase transition enthalpies. Also, the monotropic nature of the columnar phase is supported by DSC thermograms.

Further insights into the intricacies of these phases observed in complex **1**-C_{16} are provided by temperature-dependent X-ray scattering, which supports the observations of the POM. As shown in Fig. 5b, the sample during heating showed a crystal-to-LC transition at 493 K. Although several quasi-Bragg reflections were visible in the sample, the lowered intensity and broadening of the peaks, along with the shearable textures observed in POM, denoted a columnar LC phase. The peaks in the small angle region could be indexed to a two-dimensional hexagonal lattice and the lattice parameter was calculated using the relation $d_{cal} = \frac{a\sqrt{3}}{2\sqrt{h^2 + hk + k^2}}$, where (hk) are the Miller indices and a is the lattice parameter. The calculated lattice parameter was found to be a = 45.4 Å as shown in Table S11. In the wide-angle region, a broad alkyl chain correlation peak h_a (d = 4.7 Å) was observed along with a weak core-to-core stacking peak h_c (d = 3.8 Å, corroborating well with the π–π interactions between the pyridine and the pyrazolyl rings of the ligand and the subunits). An additional weak peak h_{ac} (d = 4.1 Å) was observed, which can be attributed to the partial crystallisation of the alkyl chains owing to a highly intercalated ordered structure. All these observations confirm a monotropic Col_h mesophase in complex **1**-C_{16}. During the cooling cycle, the obtained pattern (Fig. S17) remained identical up to room temperature. The intense narrow peak in the small angle region, combined with the alkyl chain-chain correlation peak and the persisting core-core interaction peak in the wide-angle region, confirm a persistent glassy columnar phase.[28–33]

The pronounced thermochromic properties and excellent solubility of the complexes in many organic solvents encouraged us to check for the possibility of thin film fabrication and investigate the effect or alteration in the magnetic and thermochromic behavior of the films compared to the bulk sample. Here, the complex **1**-C_{16} was chosen due to the presence of longer alkyl chains and the thin film was prepared by a spin-coating technique using acetonitrile solution of the complex and studied by scanning electron microscopy (SEM) (Fig. 6a and b, Fig. S18 and Table S12). The magnetic properties of the film (mechanically peeled from the glass substrate) are retained when compared with the $\chi_M T$ *vs.* T curve of the bulk powder sample (Fig. 6c). This study demonstrates the ease of

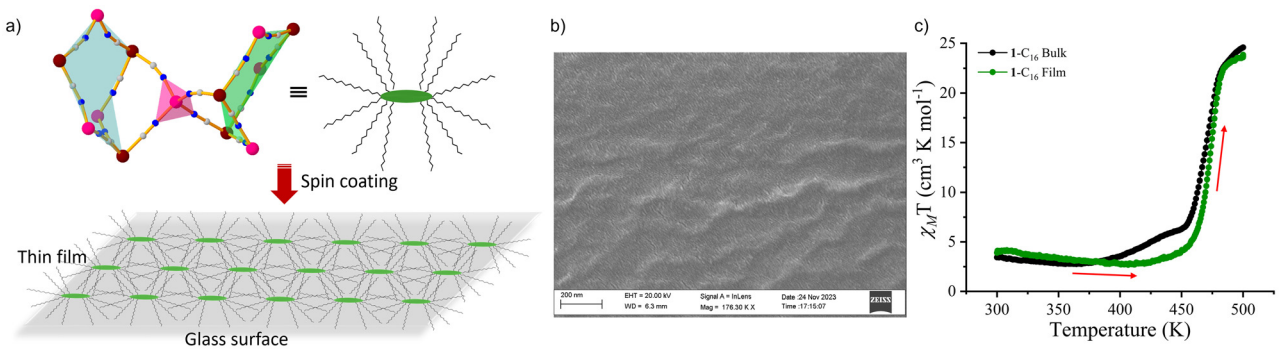

Fig. 6 (a) Plausible schematic representation of the micelle-like molecules of the complex **1**-C_{16} forming the thin film on a glass surface using the spin coating method, (b) thin film obtained from the spin coating and studied by scanning electron microscopy (SEM) and (c) $\chi_M T$ *vs.* temperature plots for the bulk and the thin film during the heating mode.

processability of the metallomesogens for thin film preparation without using the sophisticated Langmuir–Blodgett technique[12] and with no substantial deterioration of ETCST. The thermochromic behavior was also retained in the thin film which was studied by UV-visible and infrared spectroscopy studies (Fig. S19).

Conclusions

In summary, we present the first report of a series of long-chain alkylated PBAs with a tridecanuclear [Fe_6Co_7] structure, which exhibit coupled bifunctional properties: LC and ETCST, synchronised with the melting temperatures of each of the respective complexes. The magnetic transitions were accompanied by thermochromic behavior in both the solid and solution phase (green ↔ red). In the solid state, the conversion was irreversible; in contrast, it was found to be reversible in the solution phase with comparatively lower transition temperatures. The functionalisation of the complexes with long alkyl chains makes them more suitable for thin film fabrication without using any polymer matrix, and furthermore the effective shielding of the magnetic core from the surface of the substrate helps in retaining the inherent property of the complex in the thin film. Being the first report on this class of alkylated tridecanuclear PBAs, the representative compound **1**-C_{16}, the one with the highest chain length, was investigated for the LC behavior. The mesophase was inferred from three mutually exclusive studies—DSC, POM, and P-XRD. This work highlights the strategy of introducing LC behavior in PBAs to achieve the desired electronic properties, enabling new applications for these materials in electronic devices. Our group is further involved in the optimization of ligand field strength around the metal centres to tune their transitions near room temperature without compromising their LC property followed by fabrication into thin films.

Author contributions

The manuscript was written through contributions of all authors. All authors have given approval to the final version of the manuscript.

Conflicts of interest

There are no conflicts to declare.

Data availability

The data supporting this article have been included as part of the supplementary information (SI). Supplementary information: additional references.[34–42] See DOI: **https://doi.org/10.1039/d5tc03401a**.

CCDC 2348350 (complex **1**-C_4) and 2348351 (complex **2**-C_4) contain the supplementary crystallographic data for this paper.[43a,b]

Acknowledgements

J. Y. acknowledges the Council of Scientific and Industrial Research (CSIR), India for providing the Senior Research Fellowship. R. K. acknowledges PMRF for the fellowship. B. K. thanks CSIR for providing a fellowship. S. K. thanks SERB, India (Project no. CRG/2022/001676) for supporting this project. S. K., J. Y., R. K. and B. K. thank IISER Bhopal for the instrumentation facilities. S. K. P. acknowledges project file no. CRG/2019/000901/OC from DST-SERB. R. D. acknowledges IISER Mohali for the fellowship. S. K. P. and R. D. also acknowledge the SAXS/WAXS facilities at IISER Mohali.

Notes and references

1 (*a*) M. A. Halcrow, *Spin-crossover materials: properties and applications*, Wiley, Hoboken, 2013; (*b*) O. Kahn and C. J. Martinez, *Science*, 1998, **279**, 44–48.
2 (*a*) M. C. Munoz and J. A. Real, *Coord. Chem. Rev.*, 2011, **255**, 2068; (*b*) E. Coronado, *Nat. Rev. Mater.*, 2020, **5**, 87–104.
3 (*a*) P. Gutlich, A. Hauser and H. Spiering, *Angew. Chem., Int. Ed. Engl.*, 1994, **33**, 2024–2054; (*b*) P. Gutlich, Y. Garcia and H. A. Goodwin, *Chem. Soc. Rev.*, 2000, **29**, 419–427; (*c*) M. A. Halcrow, *Chem. Soc. Rev.*, 2011, **40**, 4119–4142.
4 (*a*) D. Aguila, Y. Prado, E. S. Koumousi, C. Mathoniere and R. Clerac, *Chem. Soc. Rev.*, 2016, **45**, 203–224; (*b*) Y.-S. Meng, O. Sato and T. Liu, *Angew. Chem., Int. Ed.*, 2018, **57**, 12216–12226; (*c*) J. Yadav, R. Kharel and S. Konar, *Coord. Chem. Rev.*, 2025, **525**, 216283.
5 J. A. Real, A. B. Gaspar and M. C. Munoz, *Dalton Trans.*, 2005, 2062–2079.
6 (*a*) J. Yadav, D. J. Mondal and S. Konar, *Chem. Commun.*, 2021, **57**, 5925–5928; (*b*) R. Kharel, J. Yadav and S. Konar, *Chem. Commun.*, 2024, **60**, 839–842.
7 (*a*) O. Sato, T. Iyoda, A. Fujishima and K. Hashimoto, *Science*, 1996, **272**, 704–705; (*b*) J. J. Zakrzewski, M. Liberka, J. Wang, S. Chorazy and S.-I. Ohkoshi, *Chem. Rev.*, 2024, **124**(9), 5930–6050.
8 Y. Li, A. Benchohra, B. Xu, B. Baptiste, K. Beneut, P. Parisiades, L. Delbes, A. Soyer, K. Boukheddaden and R. Lescouezec, *Angew. Chem., Int. Ed.*, 2020, **59**, 17272.
9 (*a*) I.-R. Jeon, S. Calancea, A. Panja, D. M. P. Cruz, E. S. Koumousi, P. Dechambenoit, C. Coulon, A. Wattiaux, P. Rosa, C. Mathoniere and R. Clerac, *Chem. Sci.*, 2013, **4**, 2463–2470; (*b*) J. Yadav, M. Nandi, R. Kharel, M. Mukherjee and S. Konar, *Dalton Trans.*, 2024, **53**, 8910–8914.
10 M. Cavallini, *Phys. Chem. Chem. Phys.*, 2012, **14**, 11867–11876.
11 K. S. Kumar and M. Ruben, *Coord. Chem. Rev.*, 2017, **346**, 176–205.
12 (*a*) A. B. Gaspar, M. Seredyuk and P. Gutlich, *Coord. Chem. Rev.*, 2009, **253**, 2399–2413; (*b*) Y. Galyametdinov, V. Ksenofontov, A. Prosvirin, I. Ovchinnikov, G. Ivanova, P. Gutlich and W. Haase, *Angew. Chem., Int. Ed.*, 2001, **40**, 4269–4271; (*c*) M. Seredyuk, M. C. Munoz, V. Ksenofontov, P. Gutlich,

Y. Galyametdinov and J. A. Real, *Inorg. Chem.*, 2014, **53**, 8442–8454.

13 (*a*) S. Hayami, K. Danjobara, K. Inoue, Y. Ogawa, N. Matsumoto and Y. Maeda, *Adv. Mater.*, 2004, **16**, 869–872; (*b*) S. Hayami, Y. Shigeyoshi, M. Akita, K. Inoue, K. Kato, K. Osaka, M. Takata, R. Kawajiri, T. Mitani and Y. Maeda, *Angew. Chem., Int. Ed.*, 2005, **44**, 4899–4903.

14 (*a*) S. Schlamp, B. Weber, A. D. Naik and Y. Garcia, *Chem. Commun.*, 2011, **47**, 7152–7154; (*b*) D. R.-Amorin, P. Dechambenoit, A. Bentaleb, M. Rouzieres, C. Mathoniere and R. Clerac, *J. Am. Chem. Soc.*, 2018, **140**, 98–101; (*c*) J. Weihermuller, S. Schlamp, B. Dittrich and B. Weber, *Inorg. Chem.*, 2019, **58**, 1278–1289.

15 A. B. Gaspar and M. Seredyuk, *Coord. Chem. Rev.*, 2014, **268**, 41–58.

16 (*a*) M. Seredyuk, A. B. Gaspar, V. Ksenofontov, Y. Galyametdinov, J. Kusz and P. Gutlich, *J. Am. Chem. Soc.*, 2008, **130**, 1431–1439; (*b*) J. Yadav, S. Joshi, R. De, S. K. Pal and S. Konar, *Eur. J. Inorg. Chem.*, 2024, e202400362.

17 M. Seredyuk, A. B. Gaspar, V. Ksenofontov, Y. Galyametdinov, M. Verdaguer, F. Villain and P. Gutlich, *Inorg. Chem.*, 2010, **49**, 10022–10031.

18 Y. Galyametdinov, V. Ksenofontov, A. Prosvirin, I. Ovchinnikov, G. Ivanova, P. Gutlich and W. Haase, *Angew. Chem., Int. Ed.*, 2001, **40**, 4269–4271.

19 M. Seredyuk, A. B. Gaspar, V. Ksenofontov, S. Reiman, Y. Galyametdinov, W. Haase, E. Rentschler and P. Gutlich, *Chem. Mater.*, 2006, **18**, 2513–2519.

20 S. Hayami, N. Motokawa, A. Shuto, N. Masuhara, T. Someya, Y. Ogawa, K. Inoue and Y. Maeda, *Inorg. Chem.*, 2007, **46**, 1789.

21 R. Akiyoshi, Y. Hirota, D. Kosumi, M. Tsutsumi, M. Nakamura, L. F. Lindoy and S. Hayami, *Chem. Sci.*, 2019, **10**, 5843.

22 T. Fujigaya, D. L. Jiang and T. Aida, *J. Am. Chem. Soc.*, 2003, **125**, 14690.

23 Y. Bodenthin, U. Pietsch, H. Mohwald and D. G. Kurth, *J. Am. Chem. Soc.*, 2005, **127**, 3110–3114.

24 (*a*) M. Seredyuk, A. B. Gaspar, V. Ksenofontov, S. Reiman, Y. Galyametdinov, W. Haase, E. Rentschler and P. Gutlich, *Hyperfine Interact.*, 2005, **166**, 385–390; (*b*) M. Seredyuk, A. B. Gaspar, V. Ksenofontov, Y. Galyametdinov, J. Kusz and P. Gutlich, *Adv. Funct. Mater.*, 2008, **18**, 2089–2101; (*c*) M. Seredyuk, A. B. Gaspar, V. Ksenofontov, Y. Galyametdinov, M. Verdaguer, F. Villain and P. Gutlich, *Inorg. Chem.*, 2008, **47**, 10232–10245.

25 X. Roy, L. K. Thompson, N. Coombs and M. J. MacLachlan, *Angew. Chem., Int. Ed.*, 2008, **120**, 521–524.

26 (*a*) C. Mathoniere, *Eur. J. Inorg. Chem.*, 2018, 248–258; (*b*) J. Yadav and S. Konar, *Chem. Sci.*, 2025, **16**, 130–138.

27 H. Geng, K. Luo, H. Cheng, S. Zhang, H. Ni, H. Wang, W. Yu and Q. Li, *RSC Adv.*, 2017, **7**(19), 11389–11393.

28 S. T. Trzaska and T. M. Swager, *Chem. Mater.*, 1998, **10**(1), 438–443.

29 T. Cardinaels, K. Driesen, T. N. Parac-Vogt, B. Heinrich, C. Bourgogne, D. Guillon, B. Donnio and K. Binnemans, *Chem. Mater.*, 2005, **17**(26), 6589–6598.

30 F. Morale, R. L. Finn, S. R. Collinson, A. J. Blake, C. Wilson, D. W. Bruce, D. Guillon, B. Donnio and M. Schröder, *New J. Chem.*, 2008, **32**(2), 297–305.

31 K. Venkatesan, P. H. Kouwer, S. Yagi, P. Müller and T. M. Swager, *J. Mater. Chem.*, 2008, **18**(4), 400–407.

32 F. Morale, R. W. Date, D. Guillon, D. W. Bruce, R. L. Finn, C. Wilson, A. J. Blake, M. Schröder and B. Donnio, *Chem. – Eur. J.*, 2003, **9**(11), 2484–2501.

33 G. Kinunda and D. Jaganyi, *Transition Met. Chem.*, 2016, **41**, 235–248.

34 J. Kim, S. Han, I.-K. Cho, K. Y. Choi, M. Heu, S. Yoon and B. J. Suh, *Polyhedron*, 2004, **23**, 1333–1339.

35 SAINT, *Data Reduction and Frame Integration Program for the CCD Area-Detector System. Bruker Analytical X-ray Systems*, Madison, Wisconsin, USA, 1997–2006.

36 A. Lausi, M. Polentarutti, S. Onesti, J. R. Plaisier, E. Busetto, G. Bais, L. Barba, A. Cassetta, G. Campi, D. Lamba, A. Pifferi, S. C. Mande, D. D. Sarma, S. M. Sharma and G. Paolucci, *Eur. Phys. J. Plus*, 2015, **130**, 1–8.

37 W. Kabsch, XDS, *Acta Crystallogr., Sect. D: Biol. Crystallogr.*, 2010, **66**, 125–132.

38 G. M. Sheldrick, *SHELXS-96, Program for the Solution of Crystal Structures*, University of Gottingen, Gottingen (Germany), 1996.

39 O. V. Dolomanov, L. J. Bourhis, R. J. Gildea, J. A. K. Howard and H. Puschmann, OLEX2: a complete structure solution, refinement and analysis program, *J. Appl. Crystallogr.*, 2009, **42**, 339–341.

40 G. M. Sheldrick, Crystal structure refinement with SHELXL, *Acta Crystallogr., Sect. C: Struct., Chem.*, 2015, **71**, 3–8.

41 S. Alvarez, P. Alemany, D. Casanova, J. Cirera, M. Llunell and D. Avnir, *Coord. Chem. Rev.*, 2005, **249**, 1693–1708.

42 R. Ketkaew *et al.*, *OctaDist*, 2019.

43 (*a*) CCDC 2348350: Experimental Crystal Structure Determination, 2025, DOI: **10.5517/ccdc.csd.cc2jtn78**; (*b*) CCDC 2348351: Experimental Crystal Structure Determination, 2025, DOI: **10.5517/ccdc.csd.cc2jtn89**.